

Geophysical Research Letters

RESEARCH LETTER

10.1029/2020GL088257

Key Points:

- Our work revisits the classic experiment in earthquake control at Rangely, Colorado, to determine the physical mechanism that caused these earthquakes
- The coefficient of friction for the earthquake-sourcing fault at Rangely experiment is inferred to be ~ 0.70 , consistent with Byerlee values
- We define the tectonic and anthropogenic stress contributions that caused these events, thus distinguishing “Induced” versus “Triggered” seismicity

Supporting Information:

- Supporting Information S1
- Data Set S1
- Data Set S2

Correspondence to:

J. H. Shaw,
shaw@eps.harvard.edu

Citation:

Byrne, H., Silva, J. A., Plesch, A., Juanes, R., & Shaw, J. H. (2020). The groundbreaking experiment in earthquake control at Rangely, Colorado, revisited. *Geophysical Research Letters*, 47, e2020GL088257. <https://doi.org/10.1029/2020GL088257>

Received 2 APR 2020

Accepted 11 MAY 2020

Accepted article online 16 MAY 2020

The Groundbreaking Experiment in Earthquake Control at Rangely, Colorado, Revisited

H. Byrne¹ , J. A. Silva² , A. Plesch¹ , R. Juanes^{2,3} , and J. H. Shaw¹ 

¹Department of Earth and Planetary Sciences, Harvard University, Cambridge, MA, USA, ²Department of Earth, Atmospheric and Planetary Sciences, Massachusetts Institute of Technology, Cambridge, MA, USA, ³Department of Civil and Environmental Engineering, Massachusetts Institute of Technology, Cambridge, MA, USA

Abstract Earthquakes caused by human activities are a growing societal concern. A pioneering study of induced seismicity in the 1970s involved cooperation between the U.S. Geological Survey and Chevron, Inc., to adjust operations in the Rangely oil field, Colorado, to initiate and control earthquakes. Here we revisit this experiment using coupled flow and geomechanical modeling to determine the physical mechanisms that caused these earthquakes and investigate the strength and state of stress acting on the fault that sourced them. The controlled nature of the Rangely experiment, combined with data from decades of field operations, presents a unique opportunity to understand the phenomenon of induced seismicity in ways that can be applied to manage these risks.

Plain Language Summary We revisit the classic field experiment conducted in the Rangely oil field, Colorado, to initiate and control the occurrence of earthquakes. Our study applies state-of-the-art numerical modeling to investigate the physical mechanisms that caused these events. In addition, knowledge about the structure and state of stress at Rangely from decades of field operations enables us to determine the strength of the fault and the relative contributions of tectonic versus anthropogenic stress that led to these earthquakes. These insights suggest that modest perturbations to stress fields caused by field operations can trigger seismicity on long dormant faults that are far from active tectonic plate boundaries, which has important implications for assessing and managing risks associated with induced and triggered seismicity.

1. Introduction

Earthquakes caused by human activities, known as induced seismicity, are a growing societal concern given the rapid increase in wastewater injection related to unconventional gas production and other activities (National Research Council, 2013). Dramatic increases in the frequency of seismicity in the central United States and the occurrence of recent large earthquakes in western Europe and Asia illustrate these concerns (Ellsworth, 2013; Grigoli et al., 2018; López-Comino et al., 2018; Sumy et al., 2014). To mitigate these risks, we strive for a mechanistic understanding of the phenomena that can be used to manage field operations and avoid or reduce the occurrence of these earthquakes. Toward this goal, our study revisits the classic field experiment in induced seismicity at Rangely, Colorado (Raleigh et al., 1976), using coupled flow and geomechanical modeling.

Studies of induced earthquakes can be classified into two types: those that employ a statistical approach and those that employ physics-based modeling. Studies taking a statistical approach rely on the temporal correlation of seismic and injection activities with respect to a background level of seismicity to demonstrate a link between the two (e.g., Cesca et al., 2014; Gan & Frohlich, 2013; Healy, 1968; Improta et al., 2015; Keranen et al., 2013). These studies validate many of the concerns surrounding induced seismicity but generally do not provide a mechanistic explanation of the earthquake causes and thus are limited in their capacity to inform regulations or field operating guidelines. In contrast, simulations of coupled fluid flow and geomechanics in reservoirs enable investigation of the physical processes controlling induced seismicity (Cappa & Rutqvist, 2011; Chang & Segall, 2016; Cueto-Felgueroso et al., 2017; Jha & Juanes, 2014; McClure & Horne, 2011; Pampillón et al., 2018; Torberntsson et al., 2018). Indeed, these coupled models quantify the stress changes on faults caused by anthropogenic processes, and, when calibrated by flow rate and pressure observations in wells and, where possible, additional information such as geodetic data (Jha et al., 2015),

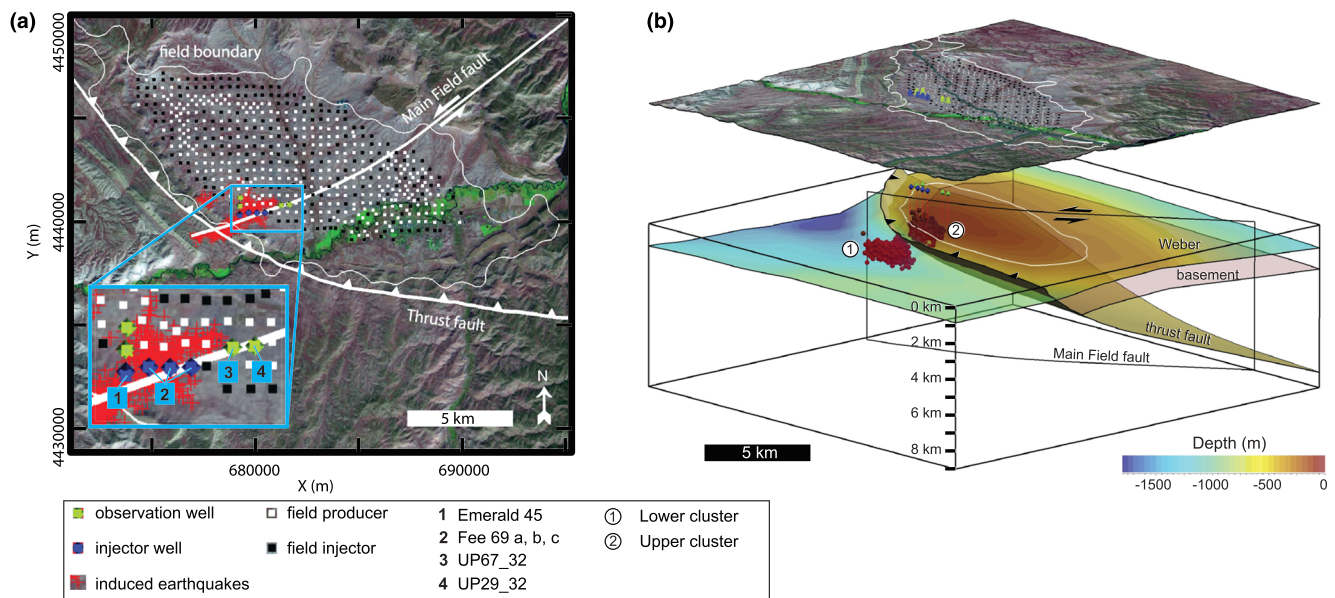


Figure 1. Geological map and model of the Rangely oil field. (a) Map (including inset of experimental focus area) and (b) perspective views of field, showing major geological elements represented in the model, wells, and seismicity induced during experiment (red spheres).

they can reproduce the physical conditions—including stress and fluid pressure changes—that may lead to seismicity, thus facilitating a mechanistic interpretation of earthquake occurrence (Andrés et al., 2019; Barbour et al., 2017; Juanes et al., 2016; Morris et al., 2011; Rinaldi & Rutqvist, 2013; Segall & Lu, 2015; Zhai et al., 2019).

The coupling between flow and stress perturbations can be described using different approaches (Dean et al., 2006; Jha & Juanes, 2014; Mainguy & Longuemare, 2002)—see the supporting information. Here we adopt a one-way coupled approach, in which the flow problem is solved first for the entire time period of interest, and the simulated pressure changes enter as internal distributed loads in the mechanics problem. A posteriori, we confirm that (1) poroelastic effects are indeed not negligible, leading to shear-stress changes on the main fault—a result that is consistent with studies of other occurrences of fluid-injection-induced seismicity (Zhai et al., 2019)—and (2) the volumetric deformation of the rock is sufficiently small that its effect on the pore pressure would not affect the conclusions, thus justifying the use of a one-way coupled model.

Here we apply these methods to examine the Rangely field experiment to determine the mechanisms, fault properties, and states of stress that control the phenomena of induced earthquakes. In particular, we explore—mechanistically and quantitatively—whether the fault sourcing the earthquakes is likely to be critically stressed, a situation that has been hypothesized to be prevalent in the Earth's crust (Townend & Zoback, 2000; Zoback, 1992).

2. The Rangely Experiment

As one of the few field-scale experiments of induced seismicity, the Rangely study tested if increases in reservoir pressure—and corresponding decreases in effective stress—acting on the faults caused their destabilization and associated earthquakes. This concept, known as the Hubbert-Rubey principle (Healy, 1968; Hsieh & Bredehoeft, 1981; Hubbert & Rubey, 1959), suggested that earthquakes may be controllable through regulation of fluid pressures.

Rangely is one of the largest and oldest oil fields in the Rocky Mountain Region. The field lies in an anticline formed during the Laramide orogeny that is associated with a thrust fault located on the southwestern boundary of the field (Figure 1a). The main producing horizon is the Pennsylvanian Weber sandstone. The primary structure within the field, known as the Main Field fault (MFF), trends northeast and has a normal offset of about 20 m (Hefner & Barrow, 1992; Mendeck, 1986). Between October 1969 and May 1974,

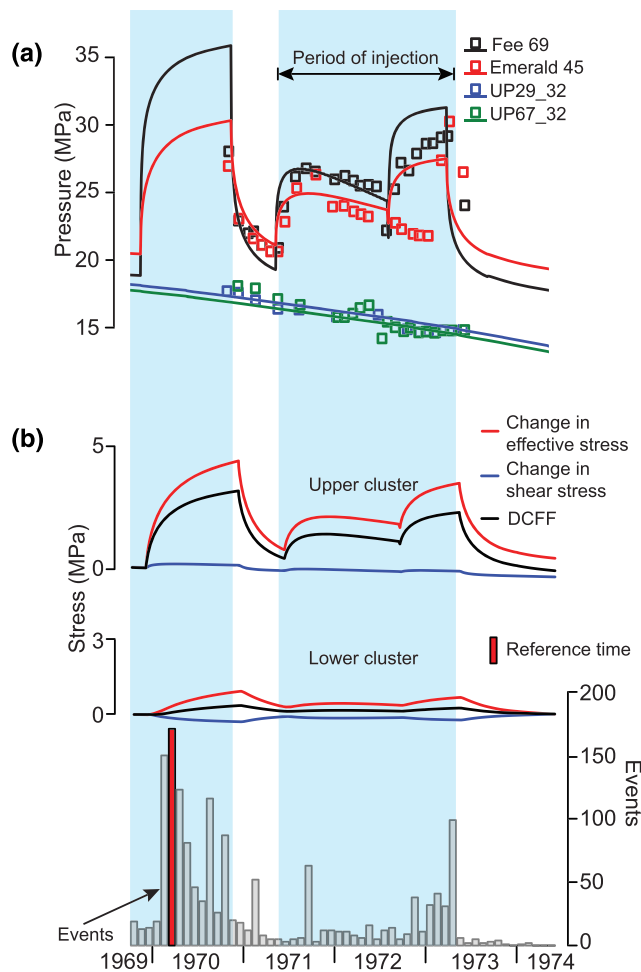


Figure 2. Evolution of pressure, stress, and CFF changes, along with earthquake history. (a) Simulated (colored lines) and measured (colored boxes) pressures at four wells used during the experiment (well locations are shown in Figure 1). The pressure readings of the Emerald45 well in 1972 were faulty as a result of leaks in that well (Raleigh et al., 1976) explaining the disparity between modeled and observed pressures during that period. (b) Evolution of changes in normal effective stress, shear stress, and DCFF at the MFF in the vicinity of the upper cluster (top) and lower cluster (middle). Increases in DCFF correspond to intense periods of earthquake activity (bottom plot), supporting the hypothesis that increases in fluid pressure destabilized the fault. The highlighted reference time corresponds to the peak earthquake rate during the first injection period and is used for our calculation of the coefficient of fault friction and stress perturbation.

and error, a process that included adjusting the injection rates at well Fee69. This calibration process, known as history matching, is a well-established standard for simulating and forecasting reservoir performance (Aziz & Settari, 1979).

The spatial and temporal evolution of pressures from the flow simulator was coupled with a geomechanical simulator, Pylith (Aagaard et al., 2013), to calculate the evolution of effective stress throughout the simulation domain, accounting for the effects of pressure changes and poroelastic coupling (Chang & Segall, 2016; Jha & Juanes, 2014). This geomechanical simulation requires imposing the tectonic stresses measured in situ within the reservoir (Haimson, 1972; Raleigh et al., 1976). We initialize our model with a prestress that is equal to the in situ stress state, and with a hydrostatic pore pressure. We then solve a boundary value problem with the following boundary conditions: zero normal displacements on all sides and bottom

operators periodically raised (through water injection) and lowered (through backflow) the reservoir pressures using four injection wells. During these periods, pressures were measured and seismicity recorded using a temporary deployment of 14 seismometers (Raleigh et al., 1976). Notably, the results indicated that seismic events on the MFF correlated spatially and temporally with zones of high pressure in the adjacent reservoir. Moreover, the operators established a pressure threshold above which earthquakes occurred and below which earthquakes largely ceased, supporting the Hubbert-Rubey principle and offering promise for controlling seismicity by managing reservoir pressures.

These results make Rangely a unique opportunity for application of coupled flow-geomechanics simulation technology (Chang & Segall, 2016; Jha & Juanes, 2014; Juanes et al., 2016). Specifically, we seek to investigate the roles of fluid pressure and poroelastic reservoir volume changes in determining the properties (permeability and friction) of the MFF and stress states that controlled the spatial and temporal evolution of the seismicity. Finally, given in situ measurements of absolute stress in the field, we seek to determine the relative contributions of anthropogenic and tectonic stresses that controlled the earthquakes.

3. Materials and Methods

To conduct our simulations, we built a computational model consisting of an unstructured 3-D mesh adapting to three stratigraphic units—the overburden, Weber sandstone, and basement—and two major faults—the vertical, N30°E trending Main Field strike-slip fault that sourced the earthquakes, underlain by the gently northeast dipping thrust fault (Figures 1 and S1). We populated this computational mesh with geologic properties. Units above the reservoir layer were assumed to be impermeable, representing Triassic strata that seal the Weber sandstone. Porosity and permeability values of the Weber unit were interpolated from well data (COGCC, 2017; Cooper, 2016) (Figure S2). To simulate reservoir operations from the Rangely experiment, we included injection wells in the model, as well as the locations of monitoring wells to compare simulated and recorded reservoir pressure.

To infer stress changes on the faults, we first simulated subsurface flow using a reservoir simulator (Jha & Juanes, 2014), honoring reservoir conditions at the onset of the experiment (October 1969), and the subsequent well injection and production schedules. We calibrated the model properties—in particular the permeability and porosity of the reservoir and the transmissibility of the MFF—to achieve a reasonable match between the simulated and measured pressures (Figure 2a). The calibration of the model to the observed pore pressure data was done manually by trial

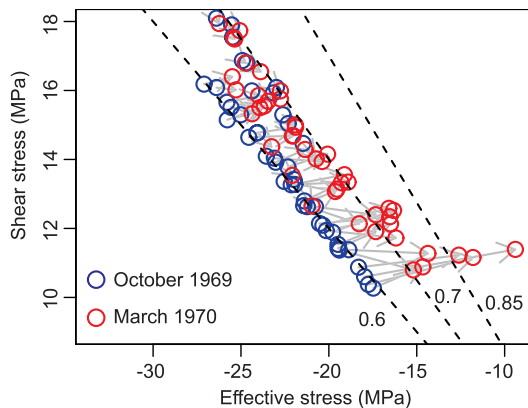


Figure 3. Change in shear stress versus normal effective stress. Blue and red circles are the state of stress on the MFF at the start of the experiment and at the reference time corresponding to the maximum earthquake rate in the first injection period, respectively. Dashed lines show values for coefficient of friction. At failure, values of normal effective stress and shear stress suggest fault coefficient of friction ≈ 0.70 . Friction calculated for other time periods during the experiment yield similar values.

boundary and zero traction on the top boundary (ground surface). Thus, our model initialization satisfies mechanical equilibrium with virtually no initial displacements and a stress state that very closely matches the prevalent tectonic stresses (Figure S3c; Table S1). These stresses are consistent with the focal mechanisms of the earthquakes reported, which suggest a right-lateral sense of slip on the MFF. Hypocenters of the events recorded in the experiment are located in distinct upper and lower clusters on the MFF, which were treated separately in the analysis (Figure 1b; Text S1).

4. Results

The effects of stress changes on fault stability are captured by the Coulomb Failure Function (CFF), defined at any point of a fault as

$$\text{CFF} = |\tau| - \mu_f (-\sigma'_n), \quad (1)$$

where τ is the shear stress, μ_f is the coefficient of friction, and σ'_n is the normal effective stress—the sum of normal total stress (negative in compression) and pore fluid pressure at that point. Changes in CFF (DCFF) that are positive denote fault destabilization. Results of the simulation

describe the changes in DCFF on the MFF during the experiment and indicate fault destabilization in both the upper and lower earthquake clusters during periods of earthquake occurrence (Figure 2b).

The regional tectonic stresses (Table S1) impose a prevalent right-lateral stress on the MFF. Reservoir expansion on the north side of the fault associated with injection causes, in addition to the direct pressurization of the fault, the following poroelastic effects (Figure S4):

1. An increase in the total normal compressive stress on the fault (blue arrows), which is stabilizing.
2. Changes in the shear stress on the fault (red arrows), with a right-lateral sense of motion to the East (which is destabilizing because it increases the right-lateral prevalent stress) and a left-lateral sense of motion to the West (which is stabilizing).

An important question is what is the magnitude of the normal and shear stress changes from the poroelastic effects relative to the direct pore pressure changes on the fault. In Figure S5 we compare these magnitudes for fault locations in the vicinity of the upper and lower clusters of seismicity. It is clear from this figure that the direct pore pressure changes on the fault are dominant for the upper cluster (Figure S5a), whereas the magnitude of the poroelastic stress changes (both normal-stress and shear-stress changes) are comparable with pressure variations in the lower cluster (Figure S5b). Thus, the results for the lower cluster of seismicity would not be replicable with an uncoupled model. While poroelastic effects are important, the contribution of the reverse coupling to the pressure variations is small (<15% see Figure S6), thus justifying the choice of a one-way coupled model.

The strength of a fault is defined by its coefficient of friction (μ_f), the ratio of shear to normal stress at which the fault will slip. Laboratory experiments have shown that μ_f can vary over time due to changes in the properties of the fault zone that occur during and between large slip events (Dieterich, 1992; Marone, 1998). However, the value of μ_f at slip initiation, referred to as the static friction, is intrinsic to the physical properties of the fault. The classic experiments of Byerlee (Byerlee, 1978) have established that μ_f for faults within a variety of rock types is remarkably consistent in laboratory experiments, with values of 0.6 to 0.85 under most conditions. However, it has proven more difficult to determine values of friction for natural faults. Some studies suggest that faults have values of friction consistent with those of Byerlee (Zoback & Townend, 2001), while others, particularly for tectonically active structures, suggest much lower values (Brune et al., 1969; Rice, 1992; Suppe, 2007). Our analysis offers a unique opportunity to calculate fault friction in situ at the time of earthquake occurrence in a well-defined stress field.

The mean value of friction is defined by the ratio of shear stress to normal effective stress (σ'_n) when the earthquake sequence initiated (Figure 3). Our study yields an average value of $\mu_f \approx 0.70$ for both clusters, similar to the Byerlee values. We hypothesize that this frictional value is higher than that reported for some tectonically active faults because the MFF has been dormant for tens of millions of years. These results suggest that natural faults may have frictional values similar to those derived from laboratory experiments, which has important implications for the magnitude of anthropogenic stress changes that might induce seismicity.

Earthquakes influenced by human activities may be of two types: induced earthquakes, where stresses acting on the fault at the time of failure are largely derived from human activities, and triggered earthquakes, where the stresses are primarily tectonic but the timing of the earthquakes is affected by anthropogenic activities (Braun et al., 2018; Cesca et al., 2012; Dahm et al., 2015; McGarr et al., 2002). This distinction has been defined conceptually, but few if any studies have been able to quantify this difference. Thus far in this article, the term “induced” has been applied to both categories. Here we seek to define the relative contributions of tectonic versus anthropogenic stress that caused these events and thus to define criteria for distinguishing between induced and triggered seismicity. We quantify the proportion of total failure stress that was introduced by anthropogenic activities using the concept of slip tendency (T_s) (Lisle & Srivastava, 2004),

$$T_s = \frac{|\tau|}{(-\sigma'_n)}. \quad (2)$$

The value of T_s equals the coefficient of friction at fault failure (when earthquakes occur) assuming no fault cohesion. Prior to fault failure, the slip tendency is less than the coefficient of friction. Our model predicts a bulls-eye pattern of T_s for the upper cluster as a result of the direct effect of pore pressure increase during the experiment, which is coincident in space and time with the upper cluster of seismicity (Figure S7a). The model predicts a more extended, spatially varying slip tendency for the lower cluster as a result of the more subtle interplay between pore pressure variations and poroelastic stresses (Figure S7b). The spatial agreement between slip tendency and earthquake locations for the lower cluster is also apparent, but less pronounced than for the upper cluster. This behavior is consistent with the smaller stress changes experienced in that region, and indicative that earthquake triggering is likely sensitive to the details of the heterogeneity in fault stresses and fault frictional properties.

The anthropogenically induced change in slip tendency can be defined as a time-dependent stress perturbation, $S_p(t)$:

$$S_p(t) = \frac{T_s(t)}{T_{s0}} - 1, \quad (3)$$

where T_{s0} is the initial slip tendency value along the fault (October 1969). From a fit to the shear and normal effective stress values on the fault, we find a value $T_{s0} \approx 0.6$ for the upper cluster (Figure 3). We calculated the stress perturbation between October 1969 and March 1970 for the two clusters of earthquakes and found disparate values: a value of 2% for the lower cluster and a value of 42% for the upper cluster, closer to the injection wells. The low stress perturbation value for the lower cluster implies that these earthquakes should be classified as “triggered”; in contrast, the high stress perturbation value for the upper cluster indicates that those earthquakes are “induced.” This quantitative classification is in accord with the conceptual view of stress alteration in the field. We consider the lower cluster to be more reflective of ambient stress state prior to field operations, due to its distance from areas of oil production. In contrast, the fault segment that sourced the upper cluster of earthquakes likely experienced fluid pressure reduction over decades of prior field development (the reservoir pressure during the experiment continues to decline, as shown by Figure 2a). Thus, the upper cluster of earthquakes may be considered induced, but largely because that segment of the fault was initially stabilized due to a prior, anthropogenically caused pressure depletion. We have no reason to believe that prior to injection the two segments of the fault, which have similar orientations, would be under very different stress states. While there is considerable uncertainty regarding the magnitude of pressure and stress changes during production, this suggests that the MFF was near the failure stress at the locations of both the upper and lower cluster of

earthquakes prior to field development, despite being long dormant and far from a tectonic plate boundary.

5. Conclusions

The coupled flow-geomechanics simulations on a geologically constrained structural model of the Rangely field, along with reservoir-pressure and seismological data, provide a unique opportunity to understand the mechanisms responsible for the observed seismicity. In particular, our analysis allows us to separate the contributions to fault destabilization from direct pore pressure diffusion and poroelastic effects and to elucidate the fundamental role of fluid flow along the fault. We synthesize the analysis by means of a metric that quantifies the anthropogenic contribution to stress perturbation, S_p , which allows us to unambiguously classify clusters of seismicity as either “triggered” or “induced”—a result that has important implications for understanding such seismicity. It is important to note that the anthropogenic stress perturbation S_p is agnostic with regard to whether the changes are from shear stress, normal stress, or pore pressure. Thus, large values of S_p —indicative of induced seismicity—can arise as a result of any combination of direct pore pressure changes and poroelastic stressing.

Our results support the hypothesis that favorably oriented faults are critically stressed throughout the crust, including tectonically inactive regions (Townend & Zoback, 2000; Zoback, 1992). This finding, supported by the derived values for fault friction, suggests that seismicity may be triggered on faults in tectonically inactive regions by even modest anthropogenic stress changes. Coupled flow and geomechanical models such as those employed in this study offer a means to investigate and potentially reduce the likelihood of such events.

Data Availability Statement

The well locations and production data used in this study are available from Raleigh et al. (1976) and the Colorado Oil and Gas Conservation Commission (COGCC) (<https://cogcc.state.co.us/#/home>). Information about fault and reservoir properties used in our model are available in Bowker and Jackson (1989), Cooper (2016), Cramer (2014), and Mendeck (1986) or can be found in the supporting information provided with this manuscript. We also include a catalog of earthquakes and a README file that describes the catalog format in the supporting information.

Acknowledgments

The authors thank Emerson for providing SKUA/Gocad software tools used in structural interpretation and property modeling. We acknowledge support of the Harvard College Research Program, Harvard University Center for the Environment and Harvard University Department of Earth and Planetary Sciences. J. A. S. and R. J. acknowledge support from ExxonMobil through the projects “Fundamentals of Induced Seismicity” and “Modeling and Mitigation of Induced Seismicity and Fault Leakage during Geological CO₂ Storage.”

References

- Aagaard, B. T., Knepley, M. G., & Williams, C. A. (2013). A domain decomposition approach to implementing fault slip in finite-element models of quasi-static and dynamic crustal deformation. *Journal of Geophysical Research: Solid Earth*, 118, 3059–3079. <https://doi.org/10.1002/jgrb.50217>
- Andrés, S., Santillán, D., Mosquera, J. C., & Cueto-Felgueroso, L. (2019). Thermo-poroelastic analysis of induced seismicity at the Basel enhanced geothermal system. *Sustainability*, 11(24), 6904. <https://doi.org/10.3390/SU11246904>
- Aziz, K., & Settari, A. (1979). *Petroleum reservoir simulation*. London: Applied Science Publishers.
- Barbour, A. J., Norbeck, J. H., & Rubinstein, J. L. (2017). The effects of varying injection rates in Osage county, Oklahoma, on the 2016 Mw 5.8 Pawnee earthquake. *Seismological Research Letters*, 88(4), 1040–1053. <https://doi.org/10.1785/0220170003>
- Bowker, K. A., & Jackson, W. D. (1989). The weber sandstone at Rangely field, Colorado. In *Sandstone Reservoirs—1989* (pp. 65–80). Denver: Rocky Mountain Association of Geologists.
- Braun, T., Cesca, S., Kühn, D., Martirosian-Janssen, A., & Dahm, T. (2018). Anthropogenic seismicity in Italy and its relation to tectonics: State of the art and perspectives. *Anthropocene*, 21, 80–94. <https://doi.org/10.1016/j.ancene.2018.02.001>
- Brune, J. N., Henyey, T. L., & Roy, R. F. (1969). Heat flow, stress, and rate of slip along the San Andreas fault, California. *Journal of Geophysical Research*, 74(15), 3821–3827. <https://doi.org/10.1029/JB074i015p03821>
- Byerlee, J. (1978). Friction of rocks. *Pure and Applied Geophysics*, 116(4-5), 615–626. <https://doi.org/10.1007/BF00876528>
- Cappa, F., & Rutqvist, J. (2011). Impact of CO₂ geological sequestration on the nucleation of earthquakes. *Geophysical Research Letters*, 38, L17313. <https://doi.org/10.1029/2011GL048487>
- Cesca, S., Dost, B., & Oth, A. (2012). Preface to the special issue “Triggered and induced seismicity: Probabilities and discrimination”. *Journal of Seismology*, 17(1), 1–4. <https://doi.org/10.1007/s10950-012-9338-z>
- Cesca, S., Grigoli, F., Heimann, S., González, Á., Bufo, E., Maghsoudi, S., et al. (2014). The 2013 September–October seismic sequence offshore Spain: A case of seismicity triggered by gas injection? *Geophysical Journal International*, 198(2), 941–953. <https://doi.org/10.1093/gji/ggu172>
- Chang, K. W., & Segall, P. (2016). Injection-induced seismicity on basement faults including poroelastic stressing. *Journal of Geophysical Research: Solid Earth*, 121, 2708–2726. <https://doi.org/10.1002/2015JB012561>
- COGCC (2017). Colorado oil and gas conservation commission. Retrieved from <https://cogcc.state.co.us/#/home>
- Cooper, J. (2016). Rangely weber sand unit WAG management optimization. In *Proc., – 20th annual CO2 flooding conference*, Midland, TX. Retrieved from <https://www.co2conference.net/wp-content/uploads/2016/12/2-Chevron-Final-2016-Midland-CO2-Forum-WAG-Optimization.pdf>

- Cramer, R. (2014). Vertical conformance, the challenge at Rangely. In *Proc., 20th annual CO2 flooding conference*, Midland, TX. Retrieved from <https://www.co2conference.net/wp-content/uploads/2016/12/2-Chevron-Final-2016-Midland-CO2-Forum-WAG-Optimization.pdf>.
- Cueto-Felgueroso, L., Santillán, D., & Mosquera, J. C. (2017). Stick-slip dynamics of flow-induced seismicity on rate and state faults. *Geophysical Research Letters*, 44, 4098–4106. <https://doi.org/10.1002/2016GL072045>
- Dahm, T., Cesca, S., Hainzl, S., Braun, T., & Krüger, F. (2015). Discrimination between induced, triggered, and natural earthquakes close to hydrocarbon reservoirs: A probabilistic approach based on the modeling of depletion-induced stress changes and seismological source parameters. *Journal of Geophysical Research: Solid Earth*, 120, 2491–2509. <https://doi.org/10.1002/2014JB011778>
- Dean, R. H., Gai, X., Stone, C. M., & Minkoff, S. E. (2006). A comparison of techniques for coupling porous flow and geomechanics. *Society of Petroleum Engineers Journal*, 11(01), 132–140. <https://doi.org/10.2118/79709-PA>
- Dieterich, J. H. (1992). Earthquake nucleation on faults with rate-and state-dependent strength. *Tectonophysics*, 211(1–4), 115–134. [https://doi.org/10.1016/0040-1951\(92\)90055-B](https://doi.org/10.1016/0040-1951(92)90055-B)
- Ellsworth, W. L. (2013). Injection-induced earthquakes. *Science*, 332(2), 250–260. <https://doi.org/10.1126/science.1234567>
- Gan, W., & Frohlich, C. (2013). Gas injection may have triggered earthquakes in the Cogdell oil field, Texas. *Proceedings of the National Academy of Sciences of the United States of America*, 110(47), 18, 786–18,791. <https://doi.org/10.1073/pnas.1311316110>
- Grigoli, F., Cesca, S., Rinaldi, A. P., Manconi, A., López-Comino, J. A., Clinton, J. F., et al. (2018). The November 2017 Mw 5.5 Pohang earthquake: A possible case of induced seismicity in South Korea. *Science*, 360(6392), 1003–1006. <https://doi.org/10.1126/science.1256789>
- Haimson, B. (1972). Earthquake related stresses at Rangely, Colorado. In *Proc., 14th U.S. Symposium on Rock Mechanics (USRMS)*, 11–14 June, University Park, Pennsylvania.
- Healy, J. H. (1968). The Denver earthquakes. *Science*, 161(3848), 1301–1310. <https://doi.org/10.1126/science.1613848.1301>
- Hefner, T. A., & Barrow, K. T. (1992). Rangely field—U.S.A. in *TR: Structural Traps VII*. Tulsa, OK: American Association Of Petroleum Geologists.
- Hsieh, P. A., & Bredehoeft, J. D. (1981). A reservoir analysis of the Denver earthquakes: A case of induced seismicity. *Journal of Geophysical Research*, 86(B2), 903–920. <https://doi.org/10.1029/JB086iB02p00903>
- Hubbert, M., & Rubey, W. W. (1959). Role of fluid pressure in mechanics of overthrust faulting: I. mechanics of fluid-filled porous solids and its application to overthrust faulting. *Bulletin of the Geological Society of America*, 70(2), 115–166. [https://doi.org/10.1130/0016-7606\(1959\)70\[115:ROFPIM\]2.0.CO;2](https://doi.org/10.1130/0016-7606(1959)70[115:ROFPIM]2.0.CO;2)
- Improta, L., Valoroso, L., Piccinini, D., & Chiarabba, C. (2015). A detailed analysis of wastewater-induced seismicity in the Val d'Agri oil field (Italy). *Geophysical Research Letters*, 42, 2682–2690. <https://doi.org/10.1002/2015GL063369>
- Jha, B., Bottazzi, F., Wojcik, R., Coccia, M., Bechor, N., McLaughlin, D., et al. (2015). Reservoir characterization in an underground gas storage field using joint inversion of flow and geodetic data. *International Journal for Numerical and Analytical Methods in Geomechanics*, 39(14), 1619–1638. <https://doi.org/10.1002/nag.2427>
- Jha, B., & Juanes, R. (2014). Coupled multiphase flow and poromechanics: A computational model of pore pressure effects on fault slip and earthquake triggering. *Water Resources Research*, 50, 3776–3808. <https://doi.org/10.1002/2013WR015175>
- Juanes, R., Jha, B., Hager, B. H., Shaw, J. H., Plesch, A., Astiz, L., et al. (2016). Were the May 2012 Emilia-Romagna earthquakes induced? A coupled flow-geomechanics modeling assessment. *Geophysical Research Letters*, 43, 6891–6897. <https://doi.org/10.1002/2016GL069284>
- Keranen, K. M., Savage, H. M., Abers, G. A., & Cochran, E. S. (2013). Potentially induced earthquakes in Oklahoma, USA: Links between wastewater injection and the 2011 Mw 5.7 earthquake sequence. *Geology*, 41(6), 699–702. <https://doi.org/10.1130/G34045.1>
- Lisle, R. J., & Srivastava, D. C. (2004). Test of the frictional reactivation theory for faults and validity of fault-slip analysis. *Geology*, 32(7), 569–572. <https://doi.org/10.1130/G20408.1>
- López-Comino, J. A., Cesca, S., Jaroslawski, J., Montcoudiol, N., Heimann, S., Dahm, T., et al. (2018). Induced seismicity response of hydraulic fracturing: Results of a multidisciplinary monitoring at the Wysin site, Poland. *Scientific Reports*, 8(1), 8653. <https://doi.org/10.1038/s41598-018-26970-9>
- Mainguy, M., & Longuemare, P. (2002). Coupling fluid flow and rock mechanics: Formulations of the partial coupling between reservoir and Geomechanical simulators. *Oil & Gas Science and Technology*, 57(4), 355–367. <https://doi.org/10.2516/ogst:2002023>
- Marone, C. (1998). Laboratory-derived friction laws and their application to seismic faulting. *Annual Review of Earth and Planetary Sciences*, 26(1), 643–696. <https://doi.org/10.1146/annurev.earth.26.1.643>
- McClure, M. W., & Horne, R. N. (2011). Investigation of injection-induced seismicity using a coupled fluid flow and rate/state friction model. *Geophysics*, 76(6), WC181–WC198. <https://doi.org/10.1190/geo2011-0064.1>
- McGarr, A., Simpson, D., & Seeber, L. (2002). 40 case histories of induced and triggered seismicity. *International Geophysics*, 81(PART A), 647–661. [https://doi.org/10.1016/S0074-6142\(02\)80243-1](https://doi.org/10.1016/S0074-6142(02)80243-1)
- Mendeck, M. F. (1986). Rangely field summary: 1. Development history and engineering data. In *New Interpretations of Northwestern Colorado Geology* (pp. 223–225). Denver, Colorado: Rocky Mountain Association of Geologists.
- Morris, J. P., Hao, Y., Foxall, W., & McNab, W. (2011). A study of injection-induced mechanical deformation at the in Salah CO2 storage project. *International Journal of Greenhouse Gas Control*, 5(2), 270–280. <https://doi.org/10.1016/j.ijggc.2010.10.004>
- National Research Council. (2013). Induced seismicity potential in energy technologies. <https://doi.org/10.17226/13355>
- Pampillón, P., Santillán, D., Mosquera, J. C., & Cueto-Felgueroso, L. (2018). Dynamic and quasi-dynamic modeling of injection-induced earthquakes in Poroelastic media. *Journal of Geophysical Research: Solid Earth*, 123, 5730–5759. <https://doi.org/10.1029/2018JB015533>
- Raleigh, C. B., Healy, J. H., & Bredehoeft, J. D. (1976). An experiment in earthquake control at Rangely, Colorado. *Science*, 191(4233), 1230–1237. <https://doi.org/10.1126/science.1914233.1230>
- Rice, J. R. (1992). Fault stress states, pore pressure distributions, and the weakness of the San Andreas Fault. *International Geophysics*, 51(C), 475–503. [https://doi.org/10.1016/S0074-6142\(08\)62835-1](https://doi.org/10.1016/S0074-6142(08)62835-1)
- Rinaldi, A. P., & Rutqvist, J. (2013). Modeling of deep fracture zone opening and transient ground surface uplift at KB-502 CO2 injection well, in Salah, Algeria. *International Journal of Greenhouse Gas Control*, 12, 155–167. <https://doi.org/10.1016/j.ijggc.2012.10.017>
- Segall, P., & Lu, S. (2015). Injection-induced seismicity: Poroelastic and earthquake nucleation effects. *Journal of Geophysical Research: Solid Earth*, 120, 5082–5103. <https://doi.org/10.1002/2015JB012060>
- Sumy, D. F., Cochran, E. S., Keranen, K. M., Wei, M., & Abers, G. A. (2014). Observations of static coulomb stress triggering of the November 2011 Mw 5.7 Oklahoma earthquake sequence. *Journal of Geophysical Research: Solid Earth*, 119, 1904–1923. <https://doi.org/10.1002/2013JB010612>
- Suppe, J. (2007). Absolute fault and crustal strength from wedge tapers. *Geology*, 35(12), 1127–1130. <https://doi.org/10.1130/G24053A.1>

- Torberntsson, K., Stiernström, V., Mattsson, K., & Dunham, E. M. (2018). A finite difference method for earthquake sequences in poroelastic solids. *Computational Geosciences*, 22(5), 1351–1370. <https://doi.org/10.1007/s10596-018-9757-1>
- Townend, J., & Zoback, M. D. (2000). How faulting keeps the crust strong. *Geology*, 28(5), 399–402. [https://doi.org/10.1130/0091-7613\(2000\)28<399:HFKTCS>2.0.CO](https://doi.org/10.1130/0091-7613(2000)28<399:HFKTCS>2.0.CO)
- Zhai, G., Shirzaei, M., Manga, M., & Chen, X. (2019). Pore-pressure diffusion, enhanced by poroelastic stresses, controls induced seismicity in Oklahoma. *Proceedings of the National Academy of Sciences*, 116(33), 16,228–16,233. <https://doi.org/10.1073/pnas.1819225116>
- Zoback, M. D., & Townend, J. (2001). Implications of hydrostatic pore pressures and high crustal strength for the deformation of intraplate lithosphere. *Tectonophysics*, 336(1–4), 19–30. [https://doi.org/10.1016/S0040-1951\(01\)00091-9](https://doi.org/10.1016/S0040-1951(01)00091-9)
- Zoback, M. L. (1992). First- and second-order patterns of stress in the lithosphere: The world stress map project. *Journal of Geophysical Research*, 97(B8), 11,703–11,728. <https://doi.org/10.1029/92JB00132>

References From the Supporting Information

- Armero, F. (1999). Formulation and finite element implementation of a multiplicative model of coupled poro-plasticity at finite strains under fully saturated conditions. *Computer Methods in Applied Mechanics and Engineering*, 171(3–4), 205–241. [https://doi.org/10.1016/S0045-7825\(98\)00211-4](https://doi.org/10.1016/S0045-7825(98)00211-4)
- Berglund, S. W. (n.d.). Trimble. Retrieved from <https://www.trimble.com/>
- de la Cruz, R. V., & Raleigh, C. B. (1972). Absolute stress measurements at the Rangely anticline, northwestern Colorado. *International Journal of Rock Mechanics and Mining Sciences*, 9(5), 625–634. [https://doi.org/10.1016/0148-9062\(72\)90013-7](https://doi.org/10.1016/0148-9062(72)90013-7)
- Jha, B., & Juanes, R. (2007). A locally conservative finite element framework for the simulation of coupled flow and reservoir geomechanics. *Acta Geotechnica*, 2(3), 139–153. <https://doi.org/10.1007/s11440-007-0033-0>
- Karimi-Fard, M., Durlöfsky, L. J., & Aziz, K. (2004). An efficient discrete-fracture model applicable for general-purpose reservoir simulators. *SPE Journal*, 9(02), 227–236. <https://doi.org/10.2118/88812-PA>
- Kim, J., Tchelepi, H. A., & Juanes, R. (2011a). Stability and convergence of sequential methods for coupled flow and geomechanics: Drained and undrained splits. *Computer Methods in Applied Mechanics and Engineering*, 200(23–24), 2094–2116. <https://doi.org/10.1016/j.cma.2011.02.011>
- Kim, J., Tchelepi, H. A., & Juanes, R. (2011b). Stability and convergence of sequential methods for coupled flow and geomechanics: Fixed-stress and fixed-strain splits. *Computer Methods in Applied Mechanics and Engineering*, 200(13–16), 1591–1606. <https://doi.org/10.1016/j.cma.2010.12.022>
- Lewis, R. W., & Sukirman, Y. (1993). Finite element modelling of three-phase flow in deforming saturated oil reservoirs. *International Journal for Numerical and Analytical Methods in Geomechanics*, 17(8), 577–598. <https://doi.org/10.1002/nag.1610170804>
- Mallet, J. L. (1992). GOCAD: A computer aided design program for geological applications. In *Three-Dimensional Modeling with Geoscientific Information Systems* (pp. 123–141). Netherlands: Springer. https://doi.org/10.1007/978-94-011-2556-7_11
- Settari, A., & Mourits, F. M. (1998). A coupled reservoir and Geomechanical simulation system. *SPE Journal*, 3(03), 219–226. <https://doi.org/10.2118/50939-PA>
- Trelis (Version 16.4). (n.d.). Retrieved from <http://csimsoft.com>
- White, J. A., Castelletto, N., & Tchelepi, H. A. (2016). Block-partitioned solvers for coupled poromechanics: A unified framework. *Computer Methods in Applied Mechanics and Engineering*, 303, 55–74. <https://doi.org/10.1016/j.cma.2016.01.008>



Geophysical Research Letters

Supporting Information for

The Groundbreaking Experiment in Earthquake Control at Rangely, Colorado revisited

H. Byrne¹, J. A. da Silva², A. Plesch¹, R. Juanes^{2,3}, J. H. Shaw¹

¹Department of Earth and Planetary Sciences, Harvard University, Cambridge, MA 02138

²Department of Earth, Atmospheric and Planetary Sciences, Massachusetts Institute of Technology, Cambridge, MA 02139

³Department of Civil and Environmental Engineering, Massachusetts Institute of Technology, Cambridge, MA 02139

Corresponding author: John Shaw (shaw@eps.harvard.edu)

Contents of this file

Text S1 to S5
Figures S1 to S7
Table S1

Additional Supporting Information (Files uploaded separately)

Data file S1

Introduction

This supplemental information describes the datasets and methods that were used in our study. All the data used in this analysis are publicly available, coming largely from other papers (as cited in the text) and online resources, such as the state of Colorado Oil and Gas Conservation Commission (COGCC, n.d.). Information on the processing of this data and the modeling methods employed in this study are summarized below.

Text S1.

Model building and parametrization

The model of the Rangely Field used for our coupled flow-geomechanics simulations integrated surface geology, well tops, and seismic reflection profiles and was developed with GOCAD (Mallet, 1992). The model includes three geologic horizons (the basement, the top Weber horizon and the Triassic seal unit) and 2 major faults (the thrust fault and strike-slip fault) (Figure 1b). The Weber reservoir horizon, with over 700 well penetrations, is highly constrained throughout the field. We used these well data and contour maps (Bowker & Jackson, 1989; Cooper, 2016.; Raleigh et al., 1976) to model the top Weber surface. The basement horizon was defined such that it maintained a constant normal distance from the Weber unit based on published cross sections and seismic reflection profiles (Cramer, 2014). Surface topography was imported from the Trimble database (Berglund, n.d.). Traces for both faults were based on the published contour maps. The thrust fault was extended to depth following the cross sections of the field (Cramer, 2014), while the strike-slip fault was extended vertically downwards, consistent with the contour maps and typical geometry of this fault type.

The model was then meshed in Trelis (Trelis (Version 16.4), n.d.). The surfaces that had been defined by nodes in GOCAD were represented as borders between solid blocks, which were defined by a series of interconnected tetrahedral elements (defined by nodes at their vertices). These solid blocks were parameterized with properties necessary to define the fluid flow and geomechanical properties of the reservoir, such as porosity and permeability (Cooper, 2016). These properties were constrained by well observations and varied as a function of depth (Figure S2). Mesh density was varied throughout the domain to give greater definition in areas of interest, such as the location of the fluid injection and the intersection of the faults.

Text S2.

Seismicity analysis

During this study, the only data on seismicity were the locations of events reported in map and cross-section in the original paper on the experiment (Raleigh et al., 1976) . In order to construct a three-dimensional catalog of earthquake locations, the data from the paper was digitized, and a Python function was used to pair corresponding points in map and cross-sectional views by minimizing the linear sum assignment. This approach worked well, uniquely identifying hypocentral locations for 949 events in the catalog. The hypocentral points were then projected onto the strike-slip fault (known to be the source of the earthquakes given the reported focal mechanisms of the events), where they occur in two evident clusters. The centroid of each cluster was located and the subsequent calculations of stress changes, coefficient of friction, and anthropogenic stress contribution are defined as being within approximately ~1500 m of the cluster centroids, which corresponds with the distributions of the hypocenters.

Text S3.**Magnitude and orientation of the primary stress at the Rangely Field**

For this study, the average maximum principal stress is taken to be in the east-west direction, as reported by (Raleigh et al., 1976). This is in agreement with the observation of right-lateral slip on the main field fault, as seen in earthquake focal mechanisms from the Raleigh experiment. The magnitudes of the principal stresses that were used in this study were estimated from analysis of hydraulic fracturing of the Weber sandstone (de la Cruz & Raleigh, 1972; Haimson, 1972; Raleigh et al., 1976; Zoback, 1992). Due to the absence of stress measurements from additional locations, stress is assumed to be laterally uniform, but depth dependent. For depth variation, ratios of principal stresses, S_1 / S_v and S_3 / S_v , where S_v is the vertical stress, were calculated from data shown in Table S1. This ratio was kept constant, while S_v was constructed through integration of smoothed density well logs available on the Colorado Oil and Gas Conservation Commission database from the top to the bottom of the finite element model (COGCC, n.d.). Depth dependent principal stresses are used as initial stresses in the coupled flow and geomechanics simulation.

Text S4.**Coupled flow–geomechanics simulations**

To solve for deformation and stresses along the Main Field fault we used a coupled flow and geomechanics simulator that honors our site-specific geological model, measured principal stresses and pore pressure evolution during the experiment.

The coupling between flow and stress perturbations can be described using different approaches (Mainguy and Longuemare, 2002; Dean et al., 2006; Jha and Juanes, 2014):

1. A *two-way coupled* model, in which the poromechanics equations are solved for both fluid pressures and rock displacements at every time step. This approach can be implemented through a simultaneous solution method (Cappa & Rutqvist, 2011; Cueto-Felgueroso et al., 2017; Jha & Juanes, 2007; Lewis & Sukirman, 1993; Zhai et al., 2019) or an iterative sequential method (Armero, 1999; Kim et al., 2011b, 2011a; Settari & Mourits, 1998; White et al., 2016). Iterative sequential approaches are desirable because they can reduce the computational cost significantly, and they offer the flexibility of using separate simulators for each subproblem.
2. A *one-way coupled* model, in which the flow problem is solved first for the entire time period of interest, and the simulated pressure changes enter as internal distributed loads in the mechanics problem. This approach assumes that the reverse coupling is negligible, but it still incorporates poroelastic effects, i.e., the impact of pressure variations on the linear momentum balance equation and expansion/compaction of the rock, leading to both normal-stress and shear-stress changes on faults.
3. An *uncoupled* model, in which the flow problem is solved first for the entire time period of interest, and poroelastic effects are neglected so that only the direct effect of pore pressure on the normal effective stress is accounted for.

Here we adopt a one-way coupled approach, and later confirm that: (1) poroelastic effects are indeed not negligible, leading to shear-stress changes on the main fault—a result that is consistent with studies of other occurrences of fluid-injection-induced seismicity (Zhai et al., 2019); (2) the volumetric deformation of the rock is sufficiently small that its effect on the pore pressure would not affect the conclusions, thus justifying the use of a one-way coupled model.

In our model, pore pressures are first obtained by history matching of the observed field pressures that accounts for the wells production and injection schedule in the Rangely oil field. This pressure

field is input into our mechanical simulator, PyLith-GPRS (Aagaard et al., 2013; Jha & Juanes, 2014), which then solves for deformation and stresses across the domain.

Since no individual well production and precise reservoir properties are available in the public domain for the Rangely oil field, we performed single-phase flow simulations and focused on reservoir pore pressure variations on the time interval of the earthquake experiment (1968 to 1976), instead of attempting to model the entire field production history from 1940's to date. When solving for pressures in the flow simulator we used spatially-varying porosities and permeabilities, based on available well information (COGCC, n.d.) (Fig. S2). The compressibility used in the fluid flow simulation is evaluated as $c = c_r + \phi c_f$, where $c_r \approx 5.5 \times 10^{-11} \text{ Pa}^{-1}$ is the rock compressibility, and $c_f \approx 3.8 \times 10^{-10} \text{ Pa}^{-1}$ is the fluid compressibility. Using a porosity $\phi = 0.15$, we obtain $c \approx 1.1 \times 10^{-10} \text{ Pa}^{-1}$. For the flow boundary conditions, we assumed that all sides of the domain are no-flow boundaries. Recognizing that the choice of boundary conditions can affect the pressure response of the system, we relied on the measured reservoir pressures in the field to calibrate our modeled pressure results, as described below. To account for the impact of the continuous production throughout the field in our simulated reservoir pressures, when the injection experiment took place, we initialized the reservoir pressures as hydrostatic and calibrated the pressure decline in the experiment area using the pressure information reported in the original Raleigh et al. (1976) paper, and we set each producing well to backflow with a flow rate equal to the total field production rate divided by the total number of producing wells. No injection rate information is available in the public domain for the injection wells used in the experiment, and therefore we manually changed the injection rates at the experimental injection wells (Fee 69a, b and c) until a good agreement was found with the reported pressures in the observation wells (Emerald 45, UP67_32, UP29_32).

We accounted for the Main Field fault in our reservoir simulation by using a discrete-fracture model that allows the definition of separate permeabilities across and along the fault (Karimi-Fard et al., 2004). Based on the measured pressures in the field during the injection experiment (Fig. 2a in the main text), we conceptualized the fault core as impermeable by setting the permeability across the fault to zero, thus isolating the wells Fee 69 and Emerald 45 from the wells UP29_32 and UP67_32. In contrast, to model the fast pore pressure communication between the injection wells and the lower cluster of earthquakes outside of the reservoir interval, we conceptualized the Main Field fault as being surrounded by a highly conductive damage zone, compared with the surrounding rocks, which was modeled by setting the permeability along the fault to be 1000 mD.

With our best history matched well pressure available, we performed a coupled flow and geomechanics analysis by using the finite element code PyLith-GPRS (Jha & Juanes, 2014). Here, we performed a one-way coupled flow simulation using the pore pressure described previously, and a Biot coefficient $b = 1$. We further assumed that the fault strength, τ_f , is always larger than the fault shear stress, τ , and thus fault slip is disallowed. In this manner, we focus only on the destabilization of the Main Field fault, using the Coulomb Failure Function (CFF), due to the combined effect of effective stress decrease (resulting from pore pressure increases) and poroelastic effects caused by the volumetric reservoir expansion. In general, faults have heterogeneous architecture and mechanical and frictional properties, which often play a significant role in determining the spatial distribution of seismic events. While these effects can be incorporated into more advanced simulation models accounting for fault slip (Chang & Segall, 2016; Cueto-Felgueroso et al., 2017; Jha & Juanes, 2014) they require precise knowledge of fault friction behavior, potentially including its spatial, temporal and slip-dependency, which are difficult to estimate.

As boundary conditions for our mechanical simulations, we fixed the bottom and the sides of the domain (Fig. S3d) and used depth-dependent initial stresses constructed based on the measured principal stresses from hydraulic fracturing at the Weber sandstone. To build these depth-dependent initial stresses, we computed the total effective vertical stress by integrating the density log (Fig. S3a, b), to compute the total vertical stress, and assuming hydrostatic pore pressure to compute the vertical effective stress. We then computed the ratio of the vertical and horizontal principal stresses using the available measured stresses from hydraulic fracturing at the Weber sandstone. By assuming that this ratio is depth-independent and, using the aforementioned vertical effective stress computed from the density log, we constructed the depth-dependent horizontal principal effective stresses (Fig. S3c). We further assumed that the vertical and horizontal principal stresses to be constant laterally throughout the field. Finally, the model was also populated with depth-dependent elastic properties based on publicly available well logs (Fig. S3a, b). We have confirmed that the domain size is sufficiently large that the presence of the boundaries does not affect the system's mechanical response (displacement and stresses) during the injection period.

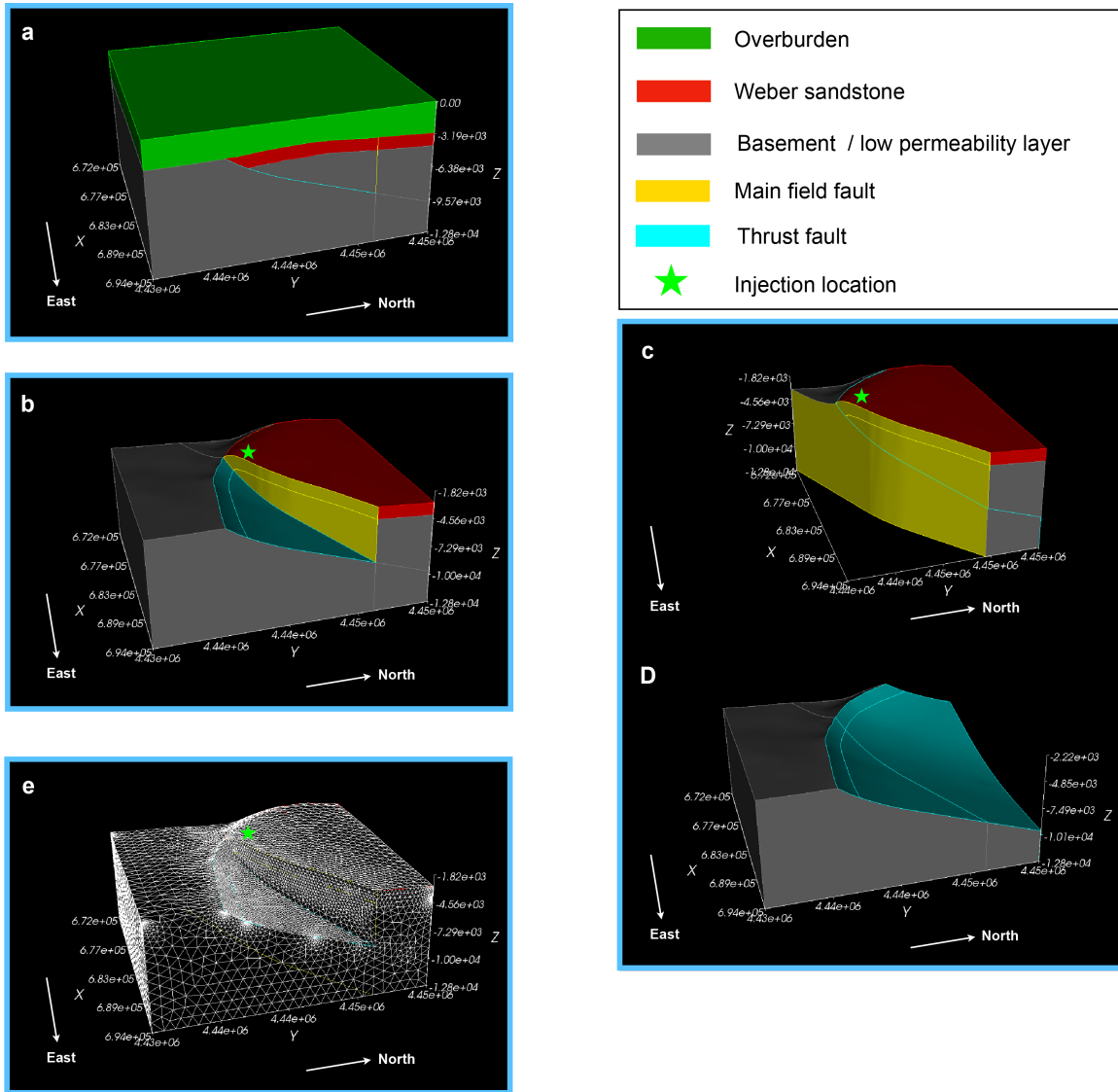


Fig. S1. Geological model and finite element mesh for the Rangely oil field. (a) Main units considered in our simulation. Green is overburden (impermeable to fluid flow), red is the Weber sandstone, and gray is the basement/low permeability layer. (b) Inside view of the geological model showing the Main Field strike-slip (yellow) and the Thrust faults (cyan). (c) Same as (b) but now focusing only on the entire Main Field strike-slip fault. (d) Same as (b) but showing the entire Thrust fault. (e) View of the finite element mesh near the Main Field Fault and the Thrust fault. Finite elements are as small as 150 m near the Main Field Fault, and increase with distance away from it.

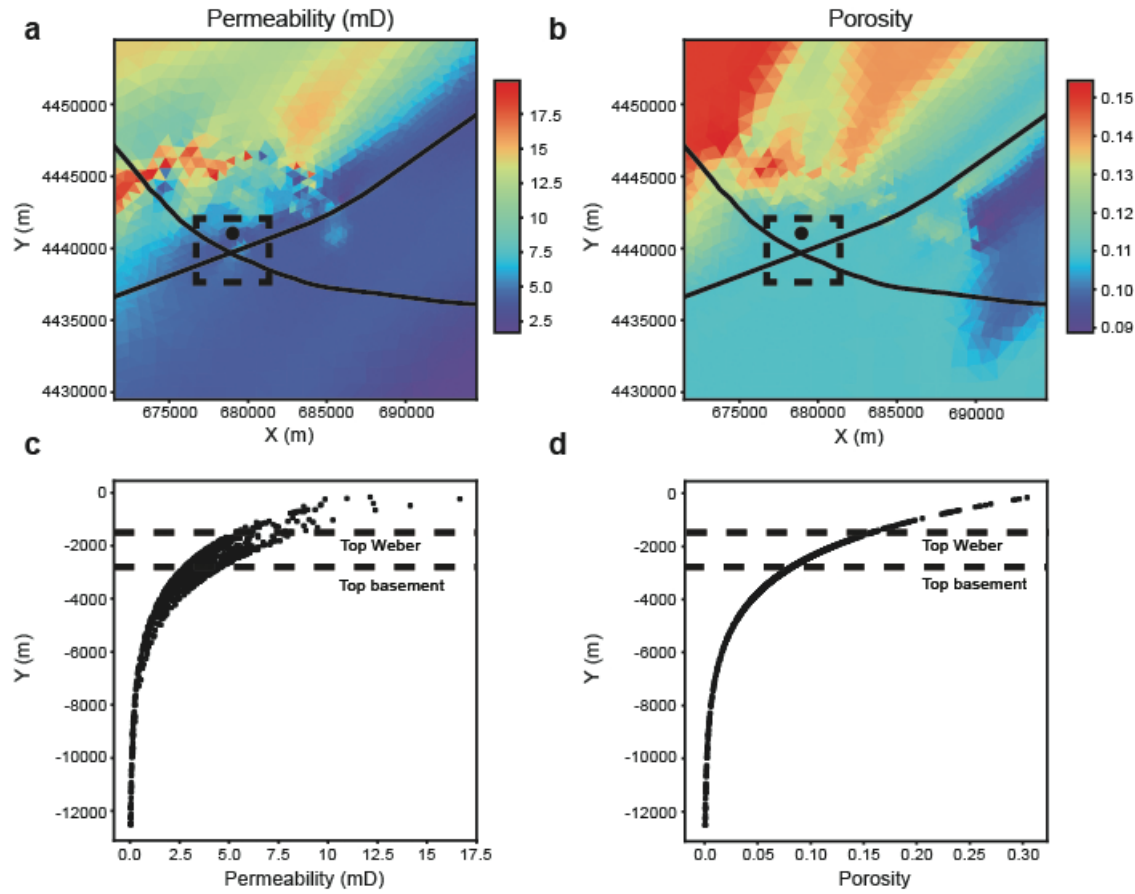


Fig. S2. Variation in permeability and porosity. (a) and (b) show the spatial variation in permeability and porosity, respectively, at the top of the Weber sandstone. Maps were constructed from the interpolation of publicly available data (Cooper, 2016). The dashed square indicates the location of the experiment and black dots represent the approximate location of injectors. Black lines represent traces of the main field and thrust faults. (c) and (d) show depth-dependent permeability and porosity, respectively, for all locations within 1 km of the black dots shown in (a) and (b). Due to a lack of publicly available data on depth-dependent variation of these properties, permeability and porosity are assumed to decay exponentially with depth, with rates that model property values at the top of the reservoir, shown in (a) and (b).

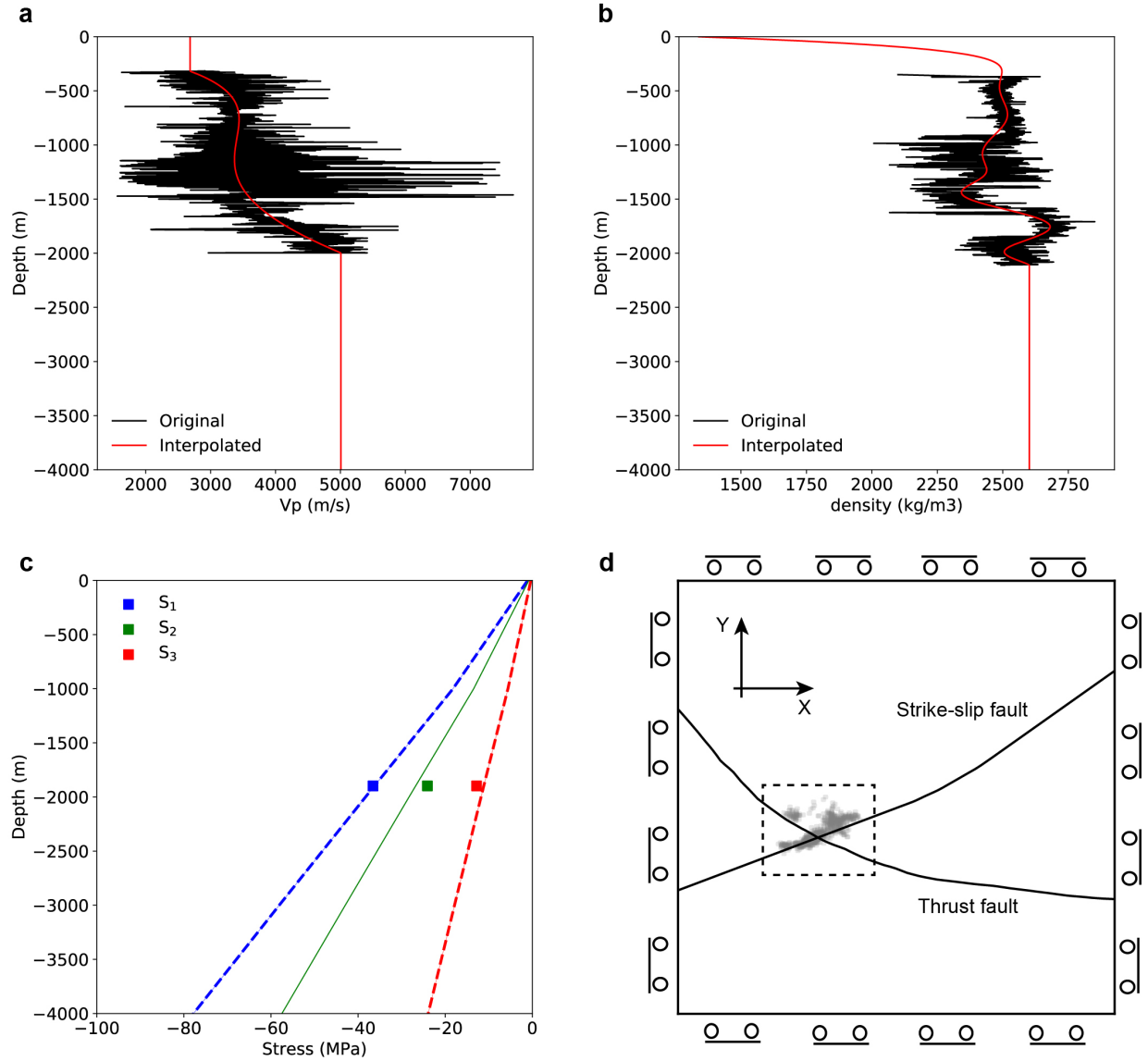


Fig. S3. Depth-dependent initial stresses and elastic properties. (a) P-wave velocity, V_p , variation with depth. Black line is the original data and red line is the smoothed version used to populate our model. We assumed a Poisson ratio of 0.25, and thus the S-wave velocity is given as $V_s = V_p/1.73$. (b) Density variation with depth, with the red line representing the smoothed version used to populate our model. (c) Depth-dependent variation of the principal effective stresses used as initial stresses in our simulations. Blue, green and red squares are principal-stress measurements from borehole hydraulic fracture at the Weber sandstone. Green solid-line is the vertical stress constructed from integration of the density curve shown in (b). The dashed-blue and dashed-red lines are the maximum and minimum principal effective stresses, respectively, constructed by keeping the ratio to the intermediate stresses constant from the observed data. (d) Model boundary conditions: zero normal displacements on all sides and bottom boundary, and zero traction on the top boundary (ground surface). The model was then initialized with the principal stresses shown in (c).

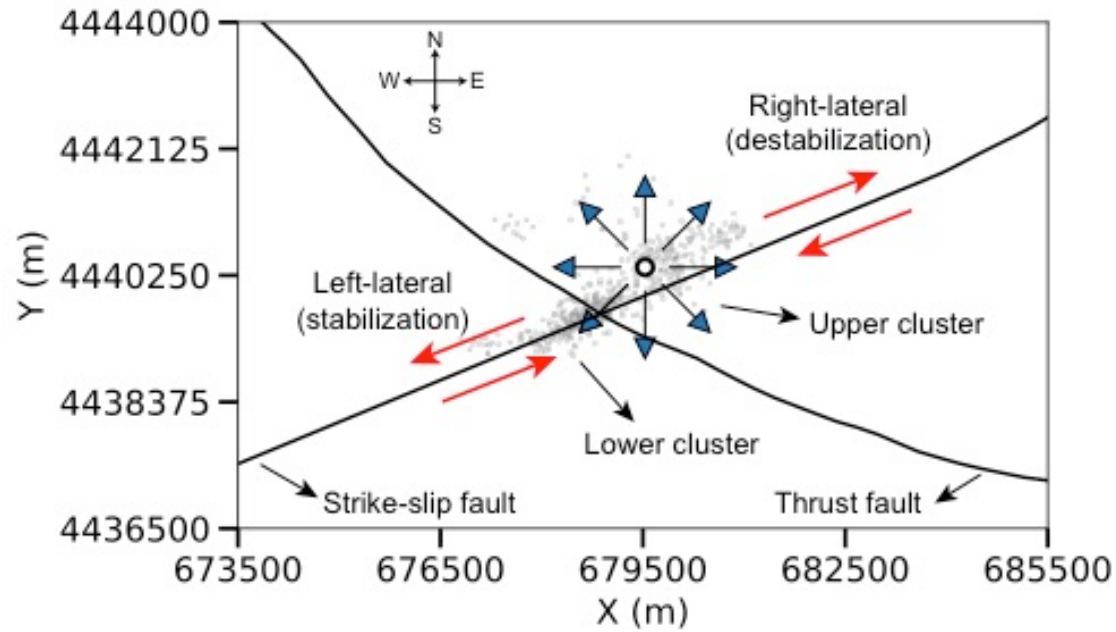


Fig. S4. Schematic of the impact of reservoir expansion from fluid injection on the stress field surrounding the injection location. Red arrows indicate the expected changes in the sense of shear stress on the Main Field Fault, which has a prevalent right-lateral stress.

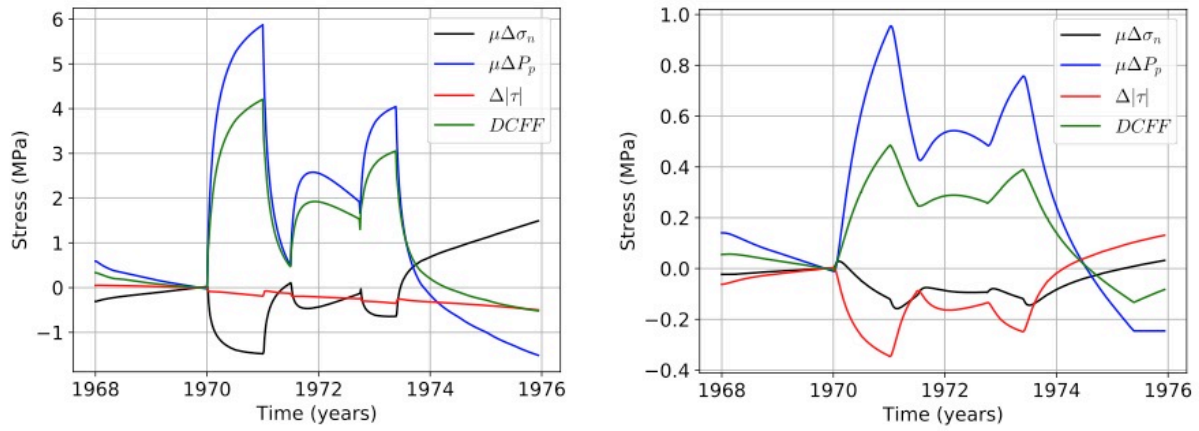


Fig. S5. Temporal evolution of the different contributions to the DCFF (green): changes in normal total stress (black), pore pressure (blue), and shear stress (red) in two different locations of the Main Field Fault. Left: vicinity of the upper cluster. Right: vicinity of the lower cluster.

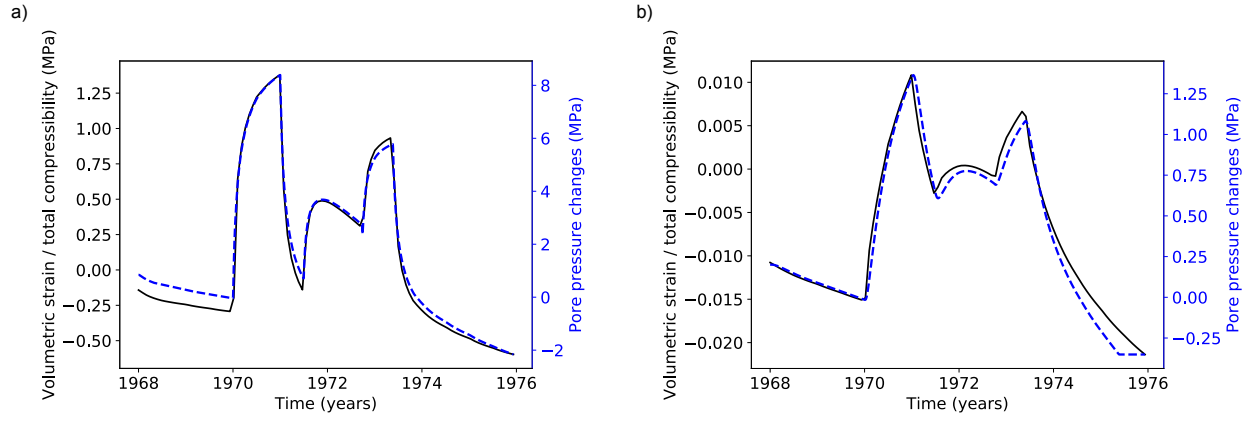


Fig. S6. Temporal evolution of changes in volumetric strain ϵ_v , and an estimate of the pore-pressure correction from the reverse poroelastic coupling $\Delta p_{rc} = \epsilon_v / c$, and comparison with the pore pressure changes Δp from the one-way coupled model in locations of the Main Field Fault: (a) vicinity of the upper cluster, (b) vicinity of the lower cluster.

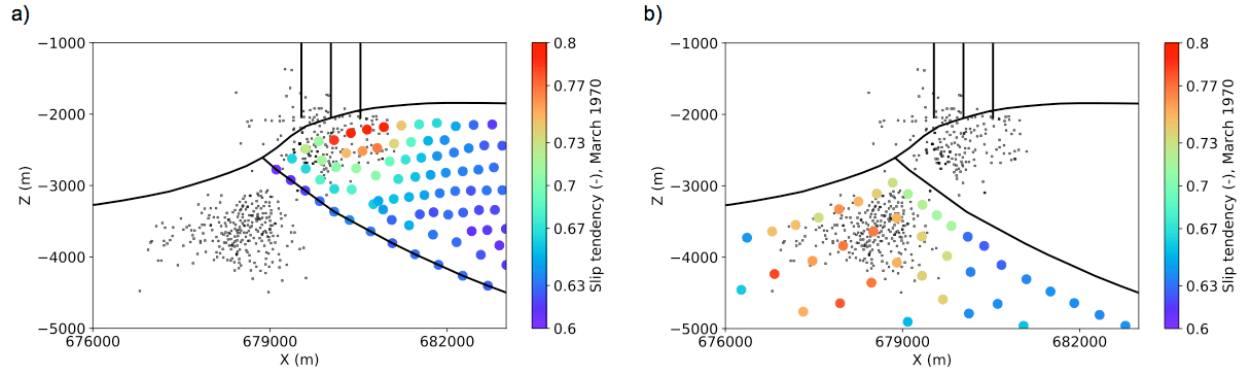


Fig. S7. Spatial variation of the slip tendency value along the Main Field Fault in March 1970 (colored circles) and its relation to the two earthquake clusters (gray circles). a) Upper cluster. b) Lower cluster.

Table S1. Magnitude and orientation of the primary stress at the Rangely Oil Field as reported by several authors.

Source	Stress magnitude (MPa)	Stress orientation	Comments
<i>Earthquake Related Stresses at Rangely, Colorado</i> (Haimson, 1972)	$S_1 = 59.0\text{MPa}$ $S_2 = 43.4\text{ MPa}$ $S_3 = 31.4\text{MPa}$	S_1 : N70°E S_2 : Vertical S_3 : N20°W	Hydraulic fracturing at 6000 ft was used with impression packing. University of Wisconsin was tasked with performing these experiments.
<i>First- and second-order patterns of stress in the lithosphere: The World Stress Map Project</i> (Zoback, 1992)		S_1 : ~ N120°E	Difficult to measure this precisely because there are several indications of maximum principal stress overlying each other. There is also no information on magnitude of the other two stresses.
<i>Absolute Stress Measurements at the Rangely Anticline, Northwestern Colorado</i> (de la Cruz & Raleigh, 1972)		S_1 : ~ N93°E	This paper compares five different methods for finding the principal stresses in the Rangely anticline. The orientation of the maximum compressive stress is an average of the results from two of the techniques at site 3 (which is the site closest to the area of interest in this study). Magnitude values vary significantly, and are orders of magnitude lower than other reported values.
<i>An Experiment in Earthquake Control at Rangely, Colorado</i> (Raleigh et al., 1976)	$S_1 = 55.2\text{MPa}$ $S_2 = 42.7\text{MPa}$ $S_3 = 31.4\text{MPa}$	S_1 : Approx. East-West S_2 : Vertical S_3 : Approx. North-South	These are the results of hydraulic fracturing tests. More weight is given to these results as they were used in the original experiment.
<i>Used in this model</i>	S_1 : 59.0MPa S_2 : 43.4 MPa S_3 : 31.4MPa	S_1 : East-West S_2 : Vertical S_3 : North-South	The magnitudes are those taken from the Haimson (1972) report. The orientations correspond to those from Raleigh et al. (1976).